First (Reflected) Light: GNSS Reflectometry on the McMurdo Ice Shelf

Seebany Datta-Barua, *Illinois Institute of Technology*
Alison F. Banwell, *University of Colorado Boulder*
Roohollah Parvizi, Arthur Baverel, Christian Allen, Alec Weedman, Logan Garcia, *Illinois Institute of Technology*
Kristine Larson, *University of Colorado Boulder*

BIOGRAPHY

Seebany Datta-Barua is a Professor of Mechanical and Aerospace Engineering at Illinois Institute of Technology. She received a Ph.D. (2008) in aeronautics and astronautics from Stanford University. Dr. Datta-Barua researches the use of GNSS for remote sensing. She was the recipient of the 2019 ION Per Enge Early Achievement Award.

Alison Banwell is a Research Scientist III in the Cooperative Institute for Research in Environmental Sciences (CIRES) at the University of Colorado Boulder. She received a Ph.D. (2013) in Glaciology from the University of Cambridge, UK. Her research focuses on understanding changes in Antarctic and Greenland ice-sheet and ice-shelf melt, hydrology, and dynamics.

Roohollah Parvizi is a Positioning Algorithm Engineer at Hemisphere GNSS. He received a Ph.D (2020) in mechanical and aerospace engineering from Illinois Institute of Technology. His current work is on detecting scintillation for real-time kinematic (RTK) positioning.

Christian Allen contributed to this work as a Mechanical Engineer at Illinois Tech. He received a Master's degree in mechanical and aerospace engineering at Illinois Institute of Technology. He is currently a Design Engineer at Hengli America Corporation, where he focuses on Cartridge Valve design.

Alec Weedman is a student research assistant pursuing his B.S. in aerospace engineering and Master's degree in mechanical and aerospace engineering at Illinois Institute of Technology. He completed the GNSS-IR data analysis and is actively working on the air brake system for the Illinois Tech Rocketry Team.

Logan Garcia is an undergraduate pursuing his B.S. in aerospace engineering at Illinois Institute of Technology. He contributed to this work during a summer research experience for undergraduates. He currently works as the deputy leader of the Spaceport Rocketry Team at Illinois Tech, as he wishes to pursue a career that pushes the boundaries of space exploration and engineering.

Kristine Larson is a Professor Emerita at the University of Colorado Boulder and National Academy Member.

ABSTRACT

The ability to monitor glaciated surface types, including snow, ice and meltwater, at a high spatial resolution, is critical for monitoring overall glacier mass balance. Using an Antarctic ice shelf as a study site, the overall goal of this work is to test the feasibility of GNSS reflectometry (GNSS-R) in monitoring glacier surfaces. During the 2023-24 Antarctic austral summer, we conducted a data campaign to collect Global Navigation Satellite System reflectometry (GNSS-R) front-end samples from two 9-m towers sited on the McMurdo Ice Shelf near McMurdo Station, Antarctica. The tower near Phoenix airfield was surrounded by snow-covered ice. The tower near the former Pegasus airfield was a heterogeneous surface of bare ice and snow-covered ice. From mid-November to early December 2023, we collected GNSS-R, camera images, and lidar data of the ice shelf surface within a 20 m radius at each of these sites. From 2-m towers with a shared field of view offset 14 m horizontally from the 9-m towers, we also collected GNSS interferometric reflectometry (GNSS-IR) data using Earthscope commercially available geodetic antenna and receiver systems. All data were returned to the lab for post-processing.

We show our first results from the site at Phoenix airfield, combining our GNSS-R estimates of surface reflectivity with the lidar and camera image data of the ice shelf surface. We find that the GNSS-R surface reflectivity is moderately positively correlated with the camera image mean red value for a snow-covered ice shelf surface. We also show GNSS-IR results from Phoenix for that day, for a satellite whose scattering zone overlaps with that of the GNSS-R zone. The reflector height estimates are robust, and lend credence to the reliability of the peak-to-noise ratio and spectral peak amplitudes. Preliminary results suggest that the spectral peak amplitude is comparable to that of the other glaciated surfaces.

I. INTRODUCTION

The cryosphere, including worldwide ice sheets and glaciers, is melting at an accelerating rate in response to Earth's warming climate (8). Therefore, it is important to be able to monitor changing glaciated surface conditions, including meltwater, as well as snow and ice-covered surfaces at high spatial resolutions, especially in order to better predict future rates of ice loss to the oceans. Antarctica is the Earth's largest ice sheet and could contribute up to 58 m of global sea-level rise if it were to melt completely. Ice shelves are the floating extensions of glaciers on land and surround about 75 percent of the Antarctic Ice Sheet (7). Ice shelves are important as they restrain glacier ice mass on land that would otherwise flow more rapidly into the ocean and contribute to sea level rise. However, Antarctica's ice shelves are thinning in response to both surface melt due to atmospheric convective heating and solar radiation, and basal melting due to warming ocean water. In turn, this means that ice shelves are weakening, diminishing their important ability to hold back inland glacier ice. Stress changes due to surface loading from melt pond development and drainage is also known to weaken and fracture ice shelves (2; 4; 3; 16; 17).

Satellite-based remote sensing usually cannot resolve surface melting at a spatial resolution that is sufficiently high to be of interest, and/or satellite-derived surface melt can usually not be validated against in-situ, ground-based observations. GNSS reflectometry leverages signals from GNSS that have reflected off surfaces to remotely sense properties of the environment. Reflectometry, particularly GNSS interferometric reflectometry (GNSS-IR), has been used in a wide variety of contexts in Earth science, including to measure snow accumulation rates in glaciated regions (13). The method is also sensitive to firn density using the vertical coordinates (13). The GNSS-IR method has been used for re-analyses of historic data, and has shown that surface heights in Antarctica can be accurately measured at about 2 cm over months and years (19; 18).

The possibility of surface ice melt monitoring using only the reflected GNSS signal from a dedicated downward-pointing antenna was previously demonstrated on a lake surface, showing moderate positive correlation with collocated georeferenced camera images of the heterogeneous lake surface. In prior fieldwork Parvizi et al. (15) collected lake ice surface data and showed a positive correlation between the GNSS signal-to-noise ratio (SNR) and the camera images' mean red value within the GNSS signal-scattering zone, used as a numerical discriminant between ice and water.

However, GNSS reflectometry data have not previously been collected from a glaciated surface. Our hypothesis was that there would be color differences between a lake surface and an ice shelf surface, especially when glacier ice is exposed (i.e. not covered by snow). Another reason to seek an ice shelf is that the glacier is flat with very open sky viewing conditions, in contrast to a mountain glacier, which will be sloped and often have other nearby mountains obscuring satellite lines-of-sight. The fact that we use GNSS-R, in addition to the more established method of GNSS-IR is useful, as this means that we can use GNSS-IR data as a baseline for comparison (13).

In this work, we ask: how does the GNSS reflectometry-based surface reflectivity compare to other measures (GNSS-IR, camera images) of the surface type for a ice shelf? For a snow-covered ice shelf, we compute the GNSS-R surface reflectivity and compare it to the mean red value of the scattering surface from collocated cameras. We plot the the GNSS-IR-derived reflector height, peak-to-noise ratio and spectral peak amplitude.

II. BACKGROUND

GNSS reflectometry is the measure of the GNSS signal after it has interacted with a surface. There are different ways of performing GNSS reflectometry, and one distinction is in considering how the incoming signal is used. In this work we use the term "reflectometry," or "GNSS-R," to refer to a system consisting of one single antenna oppositely polarized from that of the signal itself and turned upside-down, in order to collect the GNSS signal only after it has interacted with the surface. Figure 1a illustrates the concept of having a dedicated antenna for GNSS reflectometry. While a right-hand circularly polarized (RHCP) upward-facing antenna is used for positioning, a collocated downward-angled antenna of the opposite polarization of the GNSS signal is used to collect the signal after it has reflected off the surface. The single point at which the angle of incidence equals the angle of reflection is called the "specular point" (SP), but in general due to surface roughness, most energy will forward scatter from a region around the SP corresponding to the first Fresnel zone (FZ). Different surface types (e.g., ice and water in the cartoon) will scatter the signal differently, largely depending on surface roughness, compared to the wavelength of the signal being used. The measure of the signal-to-noise ratio SNR of the forward scattered signal is related to the surface reflectivity SR of the surface. The SNR is computed from the accumulated power at the correlation peak P_{max} searched over code delays and Doppler shifts, relative to the mean accumulation at the same Doppler shift for all delays beyond one half-chip on either side of the peak (15).

$$SNR = \frac{P_{max} - P_{noise}}{P_{noise}} \quad (1)$$

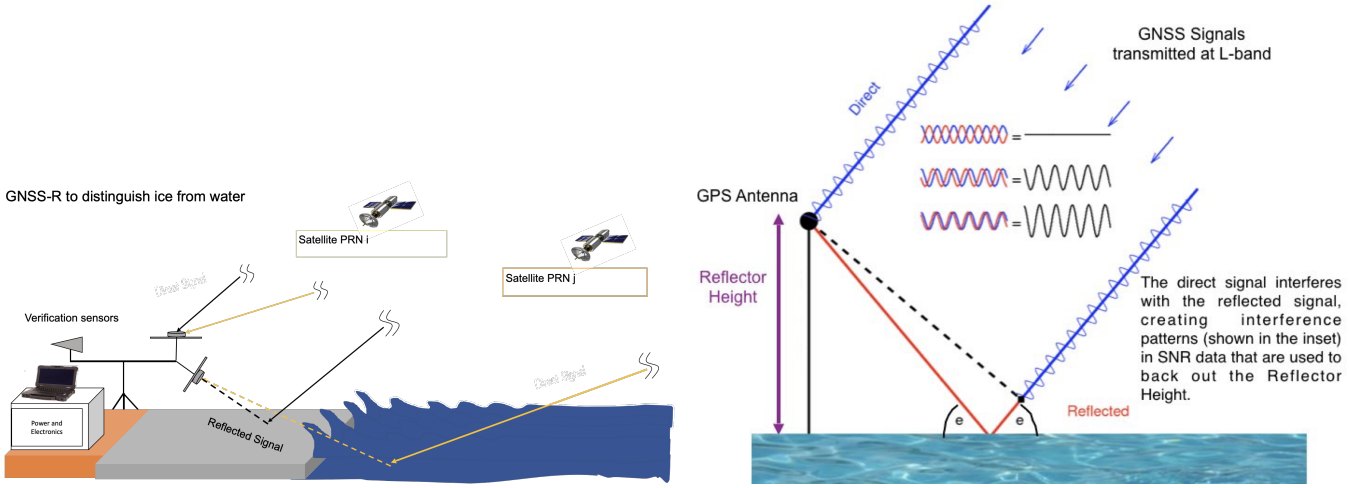

(a) Illustration of the GNSS reflectometry (GNSS-R) concept. A downward-pointing antenna receives the GNSS signal after it has interacted with the surface being sensed.

(b) Principle of GNSS interferometric reflectometry (GNSS-IR) reprinted from (12). The interference observed in the SNR time series is a function of elevation angle and reflector height.

Figure 1: Diagrams of different reflectometry architectures with GNSS.

The surface reflectivity is related to the SNR as (5):

$$SR \sim SNR - P^t - G^t - G^r - 20\log(\lambda) + 20\log(R_{ts} + R_{rs}) + 20\log(4\pi) \tag{2}$$

and depends on the transmitted power P^t, transmitter gain G^t, receiver gain G^r, wavelength λ of the signal, and the signal path lengths from the transmitter to the surface R_{ts}, and between the surface and the receive antenna R_{rs}. Given the satellite-receiver geometry and properties of the transmitter and receiver system, all the quantities on the righthand side are known. The SNR may be computed from a GNSS receiver, yielding a measure of the surface reflectivity SR. However, commercial receivers are not designed for this technique, and since the scattered signal is likely to be weak, collecting the front-end samples from the antenna with a universal software radio peripheral (USRP) and then post-processing them allows us to try various techniques to maximize the signal accumulated.

GNSS "interferometric reflectometry" (GNSS-IR) refers to the use of a single right-hand circularly polarized antenna, receiving both the direct and the multipath signal (see Fig. 1b. For satellites at low elevation, the direct and multipath signals arrive as a superposition at the antenna. As the satellite rises or sets, the signals will constructively or destructively interfere resulting in an elevation-dependent signal-to-noise ratio. The interference is a function of the reflector height H_R and satellite elevation angle el.

$$SNR(el) \quad = \quad A(el)\sin\left(\frac{4\pi H_R}{\lambda}\sin(el) + \phi\right) \tag{3}$$

A geodetic receiver with a 0 deg elevation mask can be used to collect the SNR for this purpose. A Lomb-Scargle periodogram of the SNR of a single line-of-sight rising or setting at low elevations, e.g., 5-25 degrees, can be used to estimate the reflector height. When combining the estimates from multiple lines-of-sight and estimating reflector height over days to months, GNSS-IR has been shown to be very useful for the ability to monitor tides from geodetic receivers in coastal areas, and for measuring snow accumulation on the ground surrounding a geodetic station (13).

The amplitude of the periodogram has not historically been used as much. The periodogram spectral peak amplitude is essentially a measure of the peak of the power spectral density and corresponds to the amount of signal power at the estimated reflector height. Signals scattered from a surface that is uneven over the path the Fresnel zone traverses as the satellite rises or sets will tend to lower the spectral peak amplitude and similarly the peak-to-noise ratio. The spectral peak and the peak-to-noise ratio are also a function of the surface type, as shown in examples by (12).

III. DATA COLLECTION

The objective of this work is to collect GNSS signals after they have reflected off the ice shelf, under different glaciated surface conditions (including snow, ice and meltwater), and to test whether the reflected signal varies with surface type. Two sites are selected, with differing surface types: Phoenix airfield, the current ice runway, and Pegasus, the former ice runway that has melted too much for aircraft operations since 2016. Figure 2 inset shows the Antarctic continent with the U.S. base of Antarctic operations, McMurdo Station, labeled with a red star. McMurdo Station lies on Ross Island, in the Ross Sea. Part of the Ross Sea is covered by the Ross Ice Shelf, of which a small area near to McMurdo Station is known as the McMurdo Ice Shelf. The seashore adjacent to the McMurdo Ice Shelf is known as the McMurdo Sound and is covered with sea ice, which breaks up (sometimes completely) in the Antarctic summer, unlike the ice shelf. The satellite image in Figure 2 labels McMurdo Station and the "ice shelf transition" between the seasonal sea ice and glacial ice shelf. Phoenix airfield and Pegasus airfield are labeled on the map. Parallel straight segments in the ice to the left of the Pegasus airfield label and in the snow to the left of the Phoenix Airfield label are the runways.

Red boxes label the approximate sites of the towers, sited next to the runways (Figure 2). As seen from the satellite image, taken by Sentinel-2 on 9 Nov 2023 at 10 m resolution, the two sites have generally different terrain. Phoenix is snow-covered ice shelf, and appears largely white or gray. Pegasus, on the other hand is near a region of "blue" ice, in which the ice shelf is bare, exposed to sunlight, and reflecting blue. During the melt season late December to early February, the area near Pegasus airfield has significant surface melting. The two sites were selected for their difference in surface seasonal behavior. A second factor was the relative ease of access to these sites. A groomed road is maintained between McMurdo and Phoenix, which enables wheeled vehicle access to the Phoenix tower site. The route between Phoenix and Pegasus was not maintained in the 2023-24 field season, but was still flagged from prior years and could be accessed by tracked vehicle.

Data were collected during the 2023-24 field season from mid-November to early-December. At each site, two 9-meter (30 ft) towers were established. At Phoenix (PHNX), a pre-existing 2-m tower has been in operation by EarthScope for a number of years. In order for the GNSS-R and GNSS-IR towers to be able to collect reflections from the same surfaces, the 9-m tower (77° 56' 53.17690"S, 166° 44' 41.28344" E) was placed about 14 m from the existing 2-m tower (77° 56' 52.72127" S, 166° 44' 41.24910" E). Simulations of the first Fresnel zones for two towers indicated that a north-south alignment between the towers would enable overlapping fields-of-view (FOVs), so the 9-m tower is sited about 14 m south of the existing tower. At Pegasus (PGSS) a 9-m tower (77° 57' 23.74288" S, 166° 30' 7.27981" E) and 2-m tower (77° 57' 23.64305" S, 166° 30' 9.48265" E) are sited about the same distance apart, oriented primarily east-west along the line between the Phoenix and Pegasus sites.

Figure 3a shows a schematic of the sensors used at each 9-m tower. At each site, the 9-m tower supports: one upward-facing RHCP GNSS antenna D_0 (for positioning), one downward-facing lefthand circularly polarized (LHCP) GNSS antenna for reflectometry, one lidar, and four cameras. The 9-m positioning antenna at PHNX, at PGSS and at the 2-m tower at PGSS are each Trimble Zephyrs connected to a portable Trimble NetR8 geodetic receiver with solar array mounted on the box lid. These receivers operate almost continuously for the entire period they are sited. Mounted just below the positioning antennas on the 9-m towers is the LHCP reflectometry antenna R_0. The signal from the positioning antenna is split to drive the GPS-disciplined oscillator of the USRP that serves as the GNSS-R front-end. Closer to ground level, four cameras are angled toward the ground to image the ground as near to the tower as about 3 m horizontally, and span about 300 deg azimuthal FOV around the tower. The area out of the cameras FOV is the path by which we walk to and from the base of the tower at the time of data collection. A lidar is also mounted on the tower at each site (Velodyne VLP-16 at PHNX, Ouster OS0 custom -45 deg elevation scan at PGSS), at a height such that its lowest elevation azimuthal scan reaches about 3 m away from the tower. Prior simulation of reflection zones indicated that this is the closest any GNSS-R Fresnel zone will generally reach to the base of the tower. Upon site setup, distances between instruments are measured and cameras are angled and recorded, as shown in the schematic in Fig. 3b. The schematic shows a scale model of the relative positions of the 9-m and 2-m towers. The 2-m tower hosts one upward-facing RHCP GNSS antenna I_0 (for both positioning and GNSS-IR). The pre-existing PHNX-IR upward-facing antenna is a Septentrio PolaNt connected to a Trimble NetR9 geodetic receiver (EarthScope) and powered by solar array facing north to maximize sunlight.

Figure 4 shows a photo of the Phoenix site. The surface consists of windblown snow. The 9-m tower is at right. Near the base of the left guy wires, the pre-existing PHNX 2-m tower is visible. Its solar array appears as the 2 dark rectangles near the base of the tall tower. The perimeter around the data collection zone is flagged to prevent excessive disturbance of the site. A weather station (tower at left, with a wind vane at the top) was within the perimeter of the Phoenix site as well. This was unintentional but due to the fact that the pre-existing sensors were already there and we wished to site the 9-m tower so that the GNSS-R and GNSS-IR antennas would have overlapping FOVs.

While the GNSS-R antenna, lidar, and cameras were affixed to the 9-m towers at each site for the duration of our field season (about 4 weeks), they were only powered on while we were on-site with a portable generator, an electronics box containing the USRP to collect front-end samples and supporting communication electronics, and a laptop and external storage device, all of which we transported for data collection each day of fieldwork.

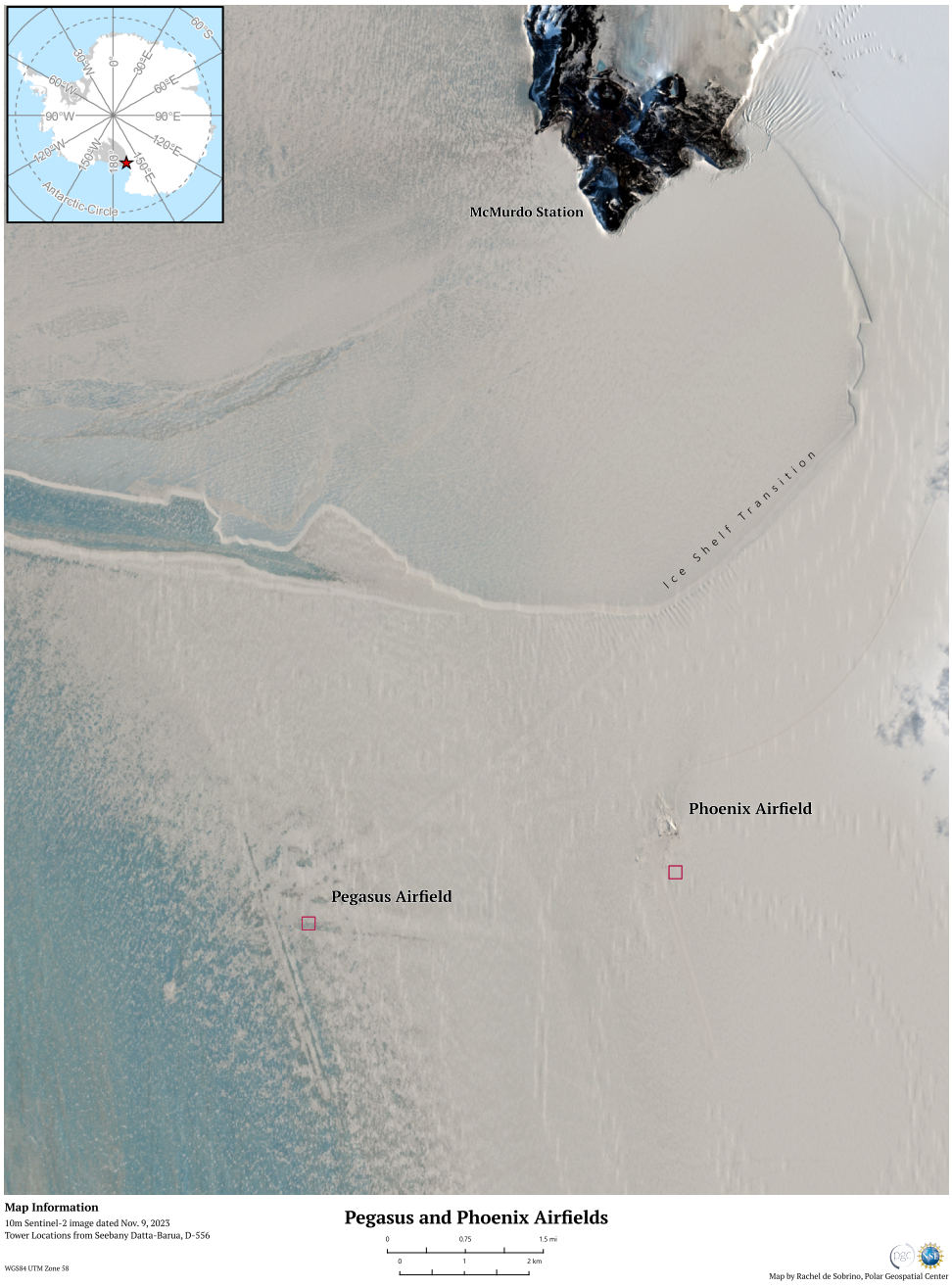

Figure 2: Satellite image of the reflectometry sites. Image credit: Rachel de Sobrino, Polar Geospatial Center. Phoenix site is at (77° 56' 53" S, 166° 44' 41.2" E). Pegasus site is at (77° 57' 23" S, 166° 30' 8" E). Inset: map of Antarctica and site of McMurdo Station and the McMurdo Ice Shelf.

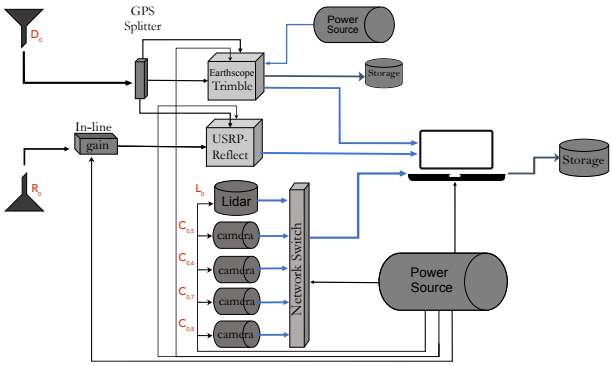

(a) Schematic of the sensor suite at each 9-m tower.

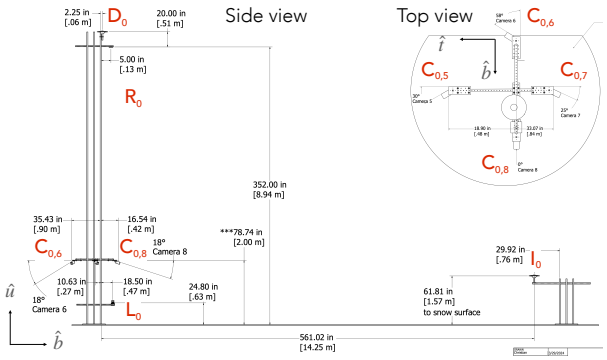

(b) Left and bottom: scale model of the PHNX-R at left and PHNX-IR towers at lower right. Top right: top-down view of the PHNX-R tower. Sensor origins are labeled in red, dimensions and angles are recorded as measured on-site.

Figure 3: Sensor diagrams and schematics.

After connecting all instruments to the electronics box and powering them one, a python script to initiate data collection from all sensors was run. We would collect data in 1-minute segments, to ensure a communication connection to all instruments was operating, alternating with 60-minute segments of data collection. Each hour of data collected yields a 72 GB GNSS-R binary file; lidar pcap file on the order of a few GB; and camera video files each on the order of about 1 GB. These data are collected on a 500 GB solid state external drive dedicated to a given site (PGSS or PHNX). Upon returning to the lab each evening, they are copied redundantly to two 10 TB storage drives, and wiped empty for the next field use.

The lidar and camera data collected in the field were inspected at the McMurdo Station lab at the end of the day for confirmation of data quality. At the end of the fieldwork period, the EarthScope team processed the Trimble data and produced raw and rinex files for our use. However, due to the file size and lack of time and processing capability, the USRP data were only examined after returning to the US.

The data shown in this work were collected during the local daytime 8 Dec 2023 (UTC + 13 h), so began at the end of 7 Dec 2023 UTC. Data were collected in multiple parts, each initiated by one run of the data collection script (called a "part"), alternatingly one-minute or an hour. At Phoenix, partway during the field season, camera 7 would error during a long data part. While its data file was readable, the remaining camera files were not. Therefore, we would in the alternating parts include one minute of all four cameras' data, followed by one part of longer duration with only cameras 5, 6 and 8 (plus the lidar and USRP, which were unaffected).

The results shown in this work based on data from the USRP R_0, the lidar, the positioning receiver D_0, and cameras 5, 6, and 8 are from the first 10 minutes of the 60 min of data collected in part 2. The PHNX 2-m tower I_0 used for GNSS-IR operated independently during this time. Because the start date of data collection was 7 Dec 2023 UT, we show GNSS-IR results from the rinex file of 7 Dec 2023, which gives the closest match in time to the satellite whose results we will show. The data collection conditions for this date are shown in Table 1. While approximate coordinates were obtained during field work, the position information for D_0, I_0 listed are based on the rinex files from the positioning receivers for that day. For camera orientation angles, the first number in a sum is the value that was measured in the field, and the second is an adjustment made manually when post-processing the data.

IV. ANALYSIS METHOD

The workflow for post-processing the data streams is shown in Fig. 5. Blue text identifies data files. Gray boxes indicate calibrations done offline separately from the processing workflow. The relative position and orientation measurements were taken in the field. The cameras were calibrated using the Matlab Camera Calibrator app in the lab after the equipment was shipped back from McMurdo to the US, following the method of Khan (10). The red text indicates the quantities that will be shown in the results.

Figure 4: Photo of experimental field site at Phoenix airfield.

The first step is to use the Trimble receivers' output Rinex 3 files to estimate positions of the GNSS-IR antenna I_0 and the tall tower D_0. To estimate the position, the Rinex files for the selected date analyzed are uploaded to the Canadian Geodetic Survey precise point positioning website (20). The resulting position estimates are listed in Table 1 for the 9-m positioning antenna (labeled D_0 in Fig. 3b) and for the GNSS-IR antenna, labeled I_0 in Fig. 3b. The website service uses the international terrestrial reference frame (ITRF), which is a realization of ITRF2020 (20). According to the National Geospatial-Intelligence Agency and the Intergovernmental Committee on Surveying and Mapping the WGS 84 TRF and ITRF are aligned at the centimeter level (Committee).

Given D_0, and the measured distances to the GNSS-R reflection antenna R_0, the coordinates of R_0 are computed. For R_0 and I_0, the satellites visible in the sky are computed based on the U.S. Coast Guard almanacs (usc). With the positions of the satellites relative to the reflectometry antennas $\vec{r}^{sv/R_0}$, $\vec{r}^{sv/I_0}$, the parameters for the specular reflection points and Fresnel zones are computed and the perimeter of the Fresnel zone points $\vec{r}^{FZ/R_0}$, $\vec{r}^{FZ/I_0}$ are computed and mapped onto a plot with the origin at R_0. Visual inspection of the map allows us to identify satellites (PRNs) that have overlapping Fresnel zones, which may allow for later comparison.

After the PRN to focus on is selected for the GNSS-R antenna, the USRP data are processed according to (15). In particular the first second of data is cropped out to remove variations in the USRP automatic gain control, then the binary data file is converted from complex to real and written out to a new file. This new file is then processed in a software defined receiver modified from Kai Borre and Jensen (9), to accumulate the signal coherently for 10 ms, then incoherently for 1 full second. The SNR is computed for this one second using Eq. (1), and repeated for each second over a full minute. The mean and standard deviation of SNR over the minute are recorded for each minute processed. Meanwhile, the position of the specular point $\vec{r}^{sp/R_0}$ is used to compute the path loss distances R_{ts}, R_{rs}. The position of the specular point from the receive antenna's zenith is also computed and an antenna gain table based on the manufacturer's antenna gain pattern is used to compute G^r. These components are used along with the previously computed SNR to compute the surface reflectivity according to Eq. (2).

The lidar and camera processing works similarly to the method of Parvizi et al. (15), with a few exceptions due to the change of geometry. We no longer crop the point cloud to points less than 2 m below and within 10 m horizontally. Instead, we take the mean of all point cloud points to compute h_1, the height of the surface below the reflected antenna.

Cameras are calibrated in the lab to determine the focal length and distortion parameters. These parameters are used to undistort each camera image. Using the lidar estimate of h_1, the images are projected back onto the surface into 3D space, interpolating

between lidar points to assign each pixel p a position vector $\vec{r}^{\,p/R_0}$ from the GNSS-R antenna. The camera orientations recorded in the field led to a mismatch in alignment of the lidar point cloud and camera images, visually identifiable by using the flagpole and solar panel features in the scene. Manual post-process adjustments are made in the software, and denoted in the second elements summed in the camera azimuth and elevation entries in Table 1.

The red value of the pixels whose points fall within the perimeter of the Fresnel zone $\vec{r}^{\,FZ/R_0}$ contribute to the calculation of the mean red value MRV within the Fresnel zone. If the entire Fresnel zone is imaged by the camera, and the satellite itself is below the downward-facing antenna's horizon, the MRV and the SR are plotted over time and a correlation coefficient is computed. In this work, unlike in Parvizi et al. (15), we plot the computed value of the SR, rather than referencing it relative to the SR at the first epoch.

The GNSS-IR processing is done using the open source gnssrefl tools available on Github (14; 11). This is a set of python tools that can be built and run with the Docker app. Given a Rinex 3 file over a 24-hour period containing SNR outputs and 0° mask angle, the tools output estimates of reflector height H_R from Eq. (3). Also provided are an estimate of the peak-to-noise ratio of the Lomb-Scargle periodogram, where the noise is defined as the mean value of the amplitude of the periodogram over the whole interval between user-selected reflector heights H_R, corresponding to wavelength as seen in Eq. (3) (12). The spectral peak amplitude is the maximum value of the spectrum. There are two quality control checks, based on exceeding user-defined threshold values of the peak-to-noise and separately the spectral peak amplitude (12). The parameters for data selection can be adjusted to output text files of the SNR for individual PRNs, whose estimates of H_R, peak-to-noise ratio and spectral peak amplitude can be plotted alone.

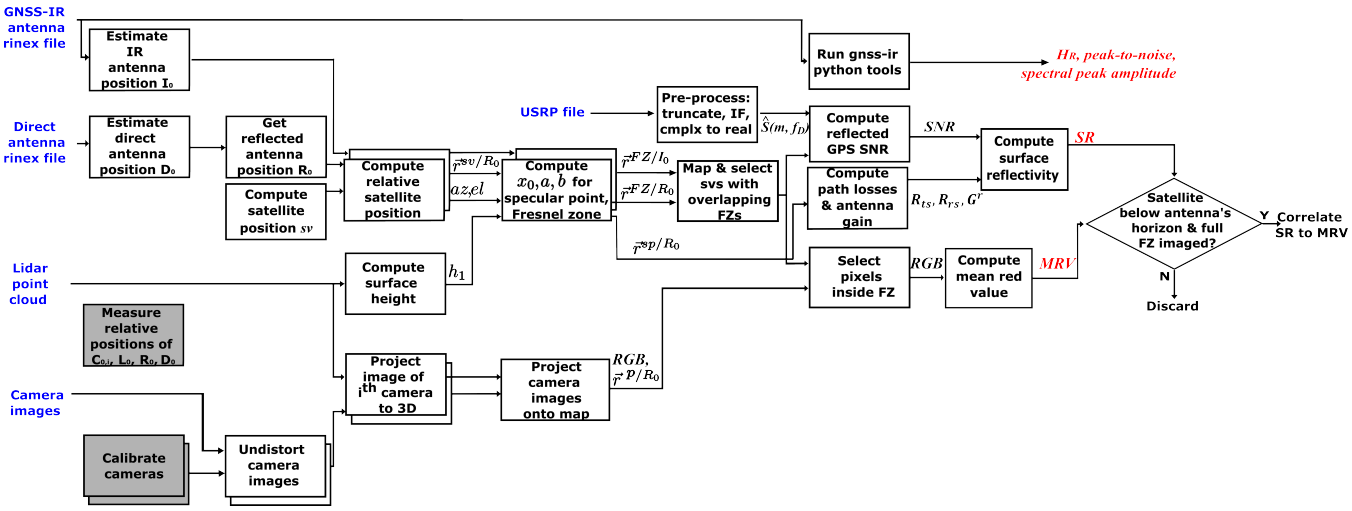

Figure 5: Post-processing workflow. Blue text identifies data files, red text identifies resulting estimates that will be shown. Gray boxes identify calibration steps that are done offline.

V. RESULTS AND DISCUSSION

The GNSS-R data analyzed were collected on local day 8 Dec 2023, part 2, beginning at 12:58PM local time (UTC + 13 hrs). One hour of data were collected from the 9-m tower, and a 24-hour data file for 7 Dec 2023 UT were collected at the 2-m tower. A sky plot at the start time of this data set is shown in Fig. 6a. From a latitude of 77° S, no satellites reach zenith, and none at the time shown have elevations higher than 60°.

The results of mapping the relative positions of the two towers, and the first Fresnel zones of the GPS satellites reflection points are shown in Figure 6b. The towers are marked with a green 'x' each, with the origin at the 9-m tower. The PHNX 2-m tower is plotted at its position relative to R_0, which is 14 m to the north of the origin. The Fresnel zones of each of the satellites above the horizon at the start of data collection (7 Dec 2023, 22:58 UT) and at the end (7 Dec 2023, 23:58 UT) are plotted as shaded ellipses. Pink ellipses correspond to the reflection zones sampled from the GNSS-R position R_0, and blue ellipses correspond to the FZs from the GNSS-IR position I_0. A set of pink and blue ellipses overlap at approximately (-2, 10) m. These correspond to PRN 11 as viewed from the 9-m tower and PRN 31 viewed from the 2-m tower. Because the towers are aligned on a north-south baseline, the satellites to the north and south of the site have an overlapping FOV sampled by their FZs. PRN 11 is selected for computing the SNR and SR from the GNSS-R data obtained with the USRP. PRN 31 is selected for viewing the peak-to-noise and spectral peak amplitude from the GNSS-IR processing of the 2-m tower data.

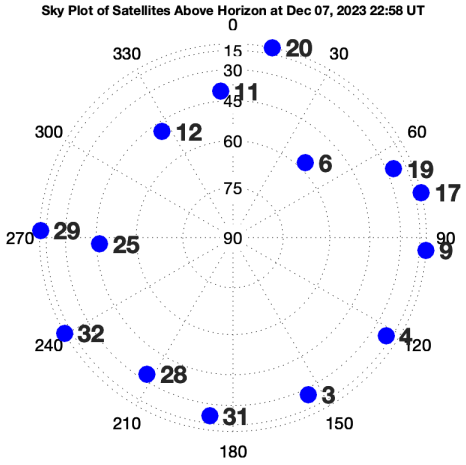

(a) Sky plot of GPS satellites in view at start of the data analyzed. PRN 11 is to the north, and PRN 31 is to the south.

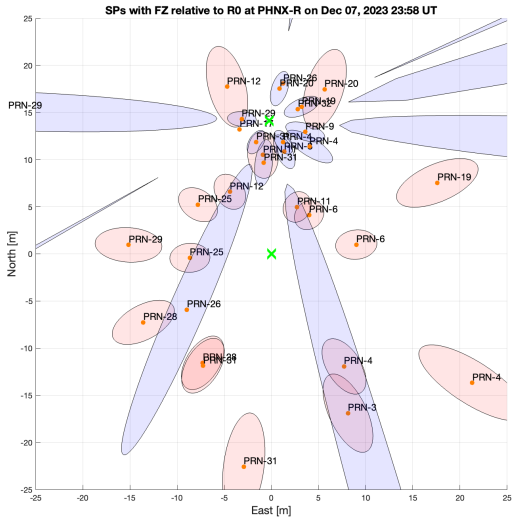

(b) Mapping of SPs and FZs at the start and end times of Part 2 of the 8 Dec 2023 data set, for selection of PRNs for reflectometry analysis. PRN 11 viewed from the 9-m tower (at origin) and PRN 31 viewed from the 2-m tower have overlapping FZs on the surface.

Figure 6: Satellite and reflection zone geometry for the local day 8 Dec 2023, Part 2, data set.

Figure 7a shows the mapping of images from cameras 5, 6 and 8 projected onto the ground using the lidar depth information. (Recall, camera 7 was shut off for the long-duration data collection in order to maintain the usability of the other three camera files.) The 9-m tower is plotted at the origin, marked with a green 'x.' Camera 8 views toward the north, which is toward the 2-m tower, as indicated in the diagram in Fig. 3b. Camera 5 views to the north east and Camera 6 to the southeast. Each pixel is projected to its location east and north on the surface based on interpolating between the nearest lidar point cloud points to the nearest camera pixel (15). We do not color-balance across the cameras, so the white of the snow in camera 8 image is more gray than the white of cameras 5 and 6. The shadow of the solar panel array is visible stretching out in the camera 8 FOV from (5, 12) m northeastward. There is some similar warping of the camera 6 image, as some blue sky pixels at (15, -10) appear to be mapped out to the ground. This is likely due to an error interpolating between near and far lidar points, in assigning a position to a pixel. Previously interpolation issues were avoided by cropping out lidar points that were beyond a certain distance from the tower (15). However, these do not affect the imaging of the first Fresnel zone of PRN 11, which is plotted in light red. The Fresnel zone of PRN 11 is entirely on a region of snow. Based on the lack of shadows within the FZ, at this location the snow appears to be relatively smooth.

Figure 7b, upper plot, shows a time series of the GNSS-R-based surface reflectivity in blue with standard deviation error bars (converted to dB), computed from the USRP front-end samples, from 22:58 UT to 23:07 UT. The mean red value of the camera pixels enclosed within the Fresnel zone ellipse at each minute over the same time is plotted in red. The lower plot shows the MRV on the horizontal axis versus the GNSS-R SR on the vertical axis. The scatter plot shows a positive correlation and these data points have a moderately positive Pearson correlation coefficient of $\rho = 0.76$. This is a similar relationship to what Parvizi et al. (15) found for a variation between lake surface ice and water.

Using the GNSS-IR open source codes (11) to process the Rinex 3 file for UT day 7 Dec 2023 from the 2-m tower gives the resulting plot shown in Fig. 8a. The top left plot shows estimates of the surface height H_R below the antenna as a function of azimuth angle of the satellite. Each circle corresponds to the estimate for the periodogram based on one PRN line-of-sight as it ranges through elevations of 5° to 25° continuously, rising or setting. Quality controls based on outliers are used to distinguish good estimates, plotted in blue, from bad (gray) ones, in which there is lower confidence. The middle plot at left shows the ratio of the periodogram peak to the noise level, with a quality control threshold defined with a dashed line. The lowest plot at left shows the spectral peak amplitude. The bad estimates in all three plots are identified as those that do not exceed the spectral peak amplitude threshold marked with the dotted line. This means the bad estimates failed the spectral peak amplitude requirement, not the peak-to-noise threshold requirement.

For this day's data set, the GNSS-IR results using L1 frequency show consistent results at all azimuth angles of the reflector height, of under 2 m. This agrees with the height measured manually in the field, of 1.57 m. In future it could also be

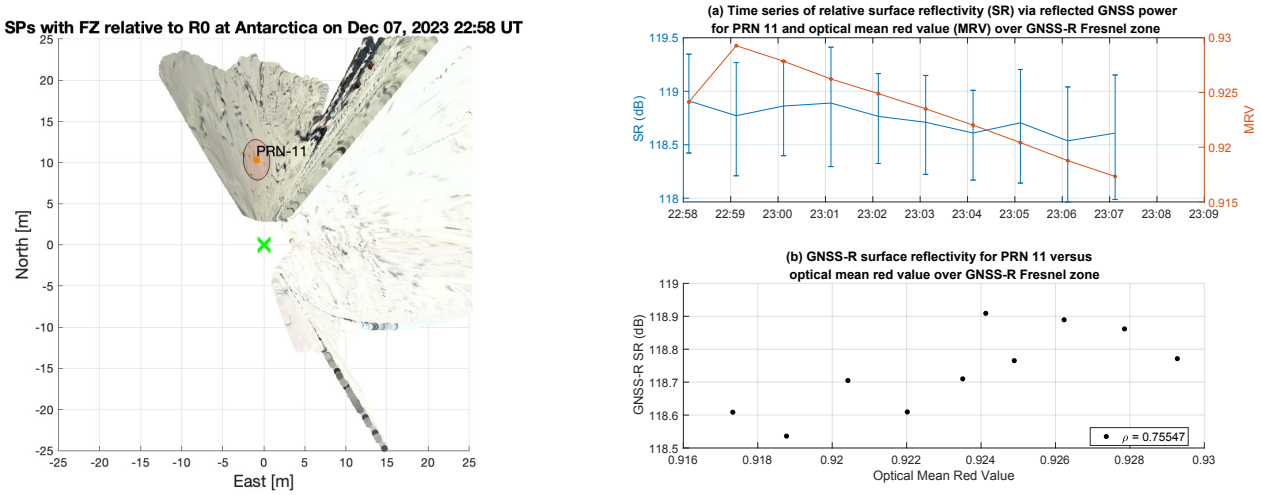

(a) FZ mapping and camera pixel selection at 22:58 UT. UT. Local time is UT plus 13 hours.

(b) (a)SR (blue) and MRV (red) over UT for PRN 11 and (b) SR versus MRV for PRN 11.

Figure 7: Comparison of GNSS-R surface reflectivity (SR) and camera image mean red value (MRV).

cross-verified with the lidar point cloud measurements, which are estimated as h_1 in the workflow in Fig. 5. The bad estimates may correspond to the reflections being obstructed by the solar panels that power the PHNX receiver, which are to its east at 90° azimuth.

For the good estimates, the peak-to-noise ratios generally exceed 4, and spectral peak amplitudes exceed 10 and in many cases are closer to 20. The higher spectral peak amplitudes are consistent with the finding demonstrated in (12), that an ice sheet surface may have an amplitude at or exceeding 20, in contrast to bare soil whose amplitude may only be 12. In this work, the ice shelf is snow-covered, which may tend to reduce the amplitude somewhat.

Since the Fresnel zone of the PRN 31 from the 2-m tower overlapped with the Fresnel zone of PRN 11 from the 9-m tower, we isolate the measurements for PRN 31 alone, in Fig. 8b. There are 4 estimates in each plot over the course of the day, each one likely corresponding to one rise or one set of the satellite, which, being in a 12-hour orbit, will rise and set in the sky twice a day. From the map in Fig. 6b, we see that the reflection zone of PRN 31 is to the south of the 2-m tower, corresponding to an azimuth angle of about 180°. This means that the estimates at azimuth of 180° correspond to those made as PRN 31 is setting to the south. This one estimate corresponds to both blue ellipses in Fig. 6b, largely spanning the FOV of PRN 11 from the 9-m tower at the first minute (pink ellipse). For the azimuth of 177.68° the estimate of reflector height based on the L1 signal is $H_R = 1.58$ m, with a peak-to-noise ratio of 5.09 and a spectral peak amplitude of about 16.69.

In this work, there is not a one-to-one comparison we can make for the GNSS-R and GNSS-IR estimates, since they have different time resolutions. However, the results shown in this work are a baseline from which we can continue to analyze the GNSS-R and GNSS-IR data at Phoenix tower for the remaining days' data (dating back to local day 19 Nov 2023). Further, this methodology will be applied in the future for the Pegasus site, which had a mix of snow-covered and bare ice. The snow-covered ice shelf measurements at Phoenix and at Pegasus will allow us to calibrate and compare between the sites.

VI. CONCLUSION

We showed preliminary results from the first GNSS-R L1 surface reflectivity experiment based on a downward-facing GPS antenna, as well as GNSS-IR data collected from the Antarctic ice shelf on UT 7 Dec 2023. The results shown were collected at two static towers 9 m and 2 m high, respectively, spaced about 14 m apart near the Phoenix airfield at McMurdo Station, Antarctica. Data collection site and procedures were also described for a second site at Pegasus, the former ice airfield. In addition to a downward facing lefthand circularly polarized antenna, the 9-m tower was equipped with an accompanying positioning antenna, lidar and cameras, which we used to map the ice shelf surface and identify the region on the surface from which the GPS signal reflected. The USRP front-end data from the GNSS-R antenna were post-processed to show that the L-band surface reflectivity from a snow-covered ice surface are positively correlated ($\rho = 0.75$) with the mean red value of camera pixels lying within the L-band reflection region. We processed Rinex 3 files from an existing receiver on a 2-m tower at Phoenix, with open source GNSS-IR tools to find a consistent and independently verified (by manual measurement) of the

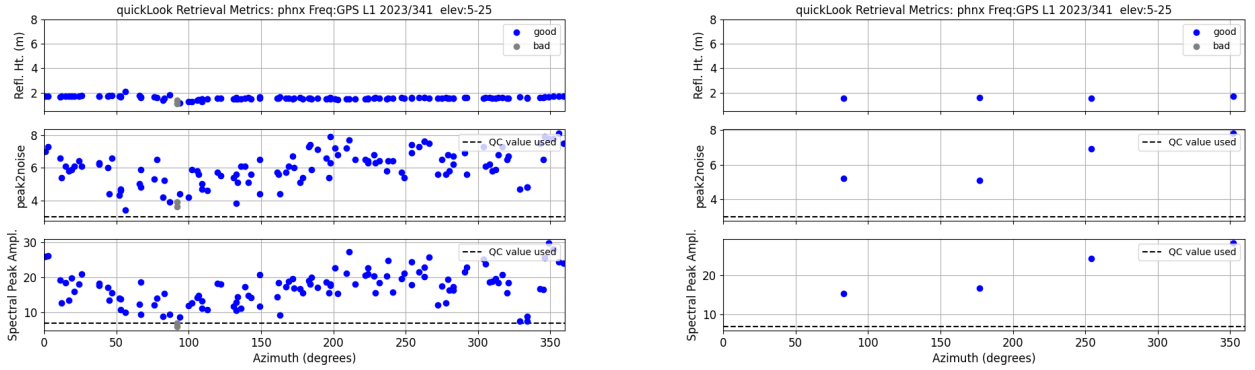

(a) Estimates based on all PRNs.

(b) Estimates based on PRN 31.

Figure 8: GNSS-IR estimates of (a) reflector height H_R, (b) peak to noise ratio, and (c) spectral peak amplitude, each as a function of the azimuthal angle, over the UT day.

surface height below the receiver, which indicates robustness of the peak-to-noise and spectral peak amplitude estimates for that day. We also isolated the estimates from the satellite whose GNSS-IR reflection zone on the surface overlaps with the GNSS-R scattering zone. These show a high spectral peak amplitude of about 17, which is closer to GNSS-IR observations of the Greenland ice sheet than of bare soil (12). Our future work includes improving the GNSS-R processing to further increase the signal-to-noise ratio on which the GNSS-R surface reflectivity measure is based; to develop a methodology for comparing among GNSS-R, GNSS-IR, and camera results; and to begin to examine the data from the Pegasus site, which includes bare ice in the vicinity of the towers.

ACKNOWLEDGEMENTS

This work was supported by the National Science Foundation Awards 1940473 and 1940483, and the NASA Illinois Space Grant Consortium. We thank Mark Seefeldt and EarthScope for the PHNX station data. The PHNX data are available at `https://www.unavco.org/instrumentation/networks/status/nota/overview/PHNX`.

The authors appreciate collaborator Doug MacAyeal for facilitating the creation of the project team and experiment concept, and for fieldwork advising. We acknowledge past students who have contributed hardware, software, or resources to this project: Shahrukh Khan, Li Pan, Lan Tran; Students of the Space Weather Lab, NavLab, and Robotics Labs at Illinois Tech. Thanks to Russ Janota, Craig Johnson, Elena Magnus, Lee Stein, and Lina Diaz of the MMAE Department for hardware and logistics. Thanks to Neel Pandya of Ettus for technical support with the USRP. For field support and implementation, we appreciate Mike Jackson, NSF; Randy Jones, Troy Juniel, Crary Lab staff, Gabe Menkhus and the riggers, EarthScope staff Erika Schreiber and Joe Pettit; Berg Field Center and Mechanical Equipment Center, and the Antarctic Services Contractors.

REFERENCES

[usc] *GPS NANUS, ALMANACS, OPS ADVISORIES, & SOF*. US. Department of Homeland Security, https://www.navcen.uscg.gov/?pageName=gpsAlmanacs.

[2] Banwell, A. F., MacAyeal, D. R., and Sergienko, O. V. (2013). Breakup of the larsen b ice shelf triggered by chain reaction drainage of supraglacial lakes. *Geophysical Research Letters*, 40(22):5872–5876.

[3] Banwell, A. F., Willis, I. C., Stevens, L. A., Dell, R. L., and MacAyeal, D. R. (2024). Observed meltwater-induced flexure and fracture at a doline on george vi ice shelf, antarctica. *Journal of Glaciology*, page 1–14.

[4] Banwell, A.F., W. I. M. G. e. a. (2019). Direct measurements of ice-shelf flexure caused by surface meltwater ponding and drainage. *Nat Commun*, 10:730.

[5] Chew, C., Reager, J. T., and Small, E. (2018). Cygnss data map flood inundation during the 2017 atlantic hurricane season. *"scientific reports"*, 8.

[Committee] Committee, C. G. R. S. Terrestrial reference frames (trf). `https://cgrsc.ca/resources/geodetic-reference-systems/terrestrial-reference-frames-trf/`.

[7] Fürst, J. J., Durand, G., Gillet-Chaulet, F., Tavard, L., Rankl, M., Braun, M., and Gagliardini, O. (2016). The safety band of antarctic ice shelves. *Nature Climate Change*, 6(5):479–482.

[8] Hanna, E., Pattyn, F., Navarro, F., Favier, V., Goelzer, H., van den Broeke, M. R., Vizcaino, M., Whitehouse, P. L., Ritz, C., Bulthuis, K., and Smith, B. (2020). Mass balance of the ice sheets and glaciers Äì progress since ar5 and challenges. *Earth-Science Reviews*, 201:102976.

[9] Kai Borre, Dennis M Akos, N. B. P. R. and Jensen, S. H. (2007). *A software-defined GPS and Galileo receiver: a single-frequency approach*. Springer Science & Business Media.

[10] Khan, S. (2020). *3D Reconstruction of Lake Surface Using Camera and Lidar Sensor Fusion*. PhD thesis, Illinois Institute of Technology.

[11] Larson, K. M. gnssrefl v3.6.8. `https://github.com/kristinemlarson/gnssrefl`.

[12] Larson, K. M. Understanding - gnssrefl documentation. Available at `https://gnssrefl.readthedocs.io/en/latest/pages/understand.html` (Accessed: 03 September 2024).

[13] Larson, K. M. (2019). Unanticipated uses of the global positioning system. *Annual Rev. Earth and Planet. Sci.*, 47:19–40.

[14] Larson, K. M. (2024). gnssrefl: an open source python software package for environmental gnss interferometric reflectometry applications. *GPS Solutions*, 28:165.

[15] Parvizi, R., Khan, S., Datta-Barua, S., and Banwell, A. F. (2024). Surface reflectivity variations of global navigation satellite signals from a mixed ice and water surface. *NAVIGATION*, 71:1.

[16] Scambos, T.A., H. C. . F. M. (2003). Climate-induced ice shelf disintegration in the antarctic peninsula. *Antarctic Research Series*, 79.

[17] Scambos, T., Fricker, H. A., Liu, C.-C., Bohlander, J., Fastook, J., Sargent, A., Massom, R., and Wu, A.-M. (2009). Ice shelf disintegration by plate bending and hydro-fracture: Satellite observations and model results of the 2008 wilkins ice shelf break-ups. *Earth and Planetary Science Letters*, 280(1):51–60.

[18] Shean, D. E., Christianson, K., Larson, K. M., Ligtenberg, S. R., Joughin, I. R., Smith, B. E., Stevens, C. M., Bushuk, M., and Holland, D. M. (2017). GPS-derived estimates of surface mass balance and ocean-induced basal melt for pine island glacier ice shelf, antarctica. *The Cryosphere*, 11(6).

[19] Siegfried, M., Medley, B., Larson, K., Fricker, H., and Tulaczyk, S. (2017). Snow accumulation variability on a west antarctic ice stream observed with GPS reflectometry, 2007–2017. *Geophysical Research Letters*, 44(15):7808–7816.

[20] Survey, C. G. (Retrieved July 11, 2024). Ppp - precise point positioning. `https://webapp.csrs-scrs.nrcan-rncan.gc.ca/geod/tools-outils/ppp.php`.

Table 1: Phoenix data collection campaign information

UT Start Time	7 Dec 2023, 22:58
D_0 Latitude	-77°, 56', 53.17690"
D_0 Longitude	166°, 44', 41.28344"
D_0 Altitude	-33.464 m
GNSS positioning make/model	Trimble NetR8
GNSS positioning antenna	Trimble Zephyr
I_0 Latitude	-77°, 56' 52.72126"
I_0 Longitude	166°, 44', 41.24910"
I_0 Altitude	-41.122 m
GNSS-IR make/model	Trimble NetR9
GNSS-IR antenna	Septentrio PolaNt
USRP make/model	Ettus N210
Reflectometry antenna	Antcom G8Ant-3A4TB1 LHCP
Lidar make/model	Velodyne VLP-16
Camera make/model (x4)	GW 5050 IP Security camera
Sampling rate	5 MHz complex
reflected USRP inline gain	40 dB
reflected USRP RF gain	31 dB
Clock used	GPS-DO
heading angle μ of the boom with respect to north	given by heading from D_0 to I_0
Relative heading angle μ_5 of camera 5	$(60+3)°$
Relative heading angle μ_6 of camera 6	$(180-58+4)°$
Relative heading angle μ_7 of camera 7	$295°$
Relative heading angle μ_8 of camera 8	$0+4.3°$
Elevation angle κ of reflected antenna	-90°
Elevation angle of lidar ψ_1	0°
Elevation angle of camera 5 ψ_5	$(-18+5)°$
Elevation angle of camera 6 ψ_6	$(-18+4.5)°$
Elevation angle of camera 7 ψ_7	$-17+0°$
Elevation angle of camera 8 ψ_8	$-18+9.7°$
Surface condition	snow-covered ice
$\vec{r}^{D_0/R_0}$	$0.07\hat{b}+0.51\hat{u}$ m
$\vec{r}^{R_0/L_0}$	$-0.34\hat{b}+8.31\hat{u}$ m
$\vec{r}^{L_0/C_{0,8}}$	$-0.05\hat{b}-1.37\hat{u}$ m
$\vec{r}^{C_{0,6}/C_{0,8}}$	$-1.22\hat{b}$ m
$\vec{r}^{C_{0,5}/C_{0,8}}$	$0.61\hat{t}-0.61\hat{b}$ m
$\vec{r}^{L_0/C_{0,7}}$	$0.61\hat{t}+1.78\hat{b}-0.15\hat{u}$ m
Camera 5 HFOV, VFOV	$73.470°, 44.760°$
Camera 6 HFOV, VFOV	$75.341°, 47.259°$
Camera 7 HFOV, VFOV	$75.341°, 47.259°$
Camera 8 HFOV, VFOV	$78.945°, 49.715°$